



**HAL**  
open science

## **Influence of the polarity of the matrix on the breakage mechanisms of lignocellulosic fibers during twin-screw extrusion**

Françoise Berzin, Loubna Lemkhanter, Carlos Marcuello Angles, Michaël Molinari, Brigitte Chabbert, Véronique Aguié-Béghin, Romain Castellani, Bruno Vergnes

### ► To cite this version:

Françoise Berzin, Loubna Lemkhanter, Carlos Marcuello Angles, Michaël Molinari, Brigitte Chabbert, et al.. Influence of the polarity of the matrix on the breakage mechanisms of lignocellulosic fibers during twin-screw extrusion. *Polymer Composites*, 2020, 41 (3), pp.1106-1117. 10.1002/pc.25442 . hal-04057893

**HAL Id: hal-04057893**

**<https://hal.science/hal-04057893>**

Submitted on 4 Apr 2023

**HAL** is a multi-disciplinary open access archive for the deposit and dissemination of scientific research documents, whether they are published or not. The documents may come from teaching and research institutions in France or abroad, or from public or private research centers.

L'archive ouverte pluridisciplinaire **HAL**, est destinée au dépôt et à la diffusion de documents scientifiques de niveau recherche, publiés ou non, émanant des établissements d'enseignement et de recherche français ou étrangers, des laboratoires publics ou privés.



**Influence of the polarity of the matrix on the breakage mechanisms of lignocellulosic fibers during twin-screw extrusion**

Journal:	<i>Polymer Composites</i>
Manuscript ID	PC-19-0869.R1
Wiley - Manuscript type:	Research Article
Date Submitted by the Author:	n/a
Complete List of Authors:	Berzin, Françoise; Universite de Reims Champagne-Ardenne, Lemkhanter, Loubna; INRA, FARE Marcuello, Carlos; INRA, FARE Chabbert, Brigitte; INRA, FARE Aguié-Béghin, Véronique ; INRA, FARE Molinari, Michael; University of Bordeaux Castellani, Romain; Mines ParisTech Sophia Antipolis, CEMEF Vergnes, Bruno; MINES ParisTech, CEMEF
Keywords:	fibers, rheology, adhesion, atomic force microscopy (AFM), compounding

SCHOLARONE™  
Manuscripts

1  
2  
3 **Influence of the polarity of the matrix on the breakage mechanisms of**  
4  
5  
6 **lignocellulosic fibers during twin-screw extrusion**  
7

8 **Running title: Breakage mechanism of lignocellulosic fibers**  
9

10  
11  
12  
13 **Françoise Berzin<sup>a</sup>, Loubna Lemkhanter<sup>a</sup>, Carlos Marcuello<sup>a</sup>, Brigitte Chabbert<sup>a</sup>,**  
14  
15 **Véronique Aguié-Béghin<sup>a</sup>, Michael Molinari<sup>b</sup>, Romain Castellani<sup>c</sup>, Bruno Vergnes<sup>c</sup>**  
16  
17  
18  
19

20  
21 <sup>a</sup> Université de Reims Champagne Ardenne, INRA, FARE, UMR A 614, 51100 Reims,  
22  
23 France  
24

25 <sup>b</sup> CBMN, UMR CNRS 5248, Université de Bordeaux, INP Bordeaux, 33600 Pessac, France  
26  
27

28 <sup>c</sup> MINES ParisTech, PSL Research University, CEMEF (Centre de Mise en Forme des  
29  
30 Matériaux), UMR CNRS 7635, CS 10207, 06904 Sophia Antipolis Cedex, France  
31  
32  
33  
34

35 Corresponding author:  
36

37  
38 Bruno Vergnes  
39

40 MINES ParisTech, PSL Research University, CEMEF (Centre de Mise en Forme des  
41 Matériaux),  
42 UMR CNRS 7635, CS 10207, 06904 Sophia Antipolis Cedex (France)  
43

44 [bruno.vergnes@mines-paristech.fr](mailto:bruno.vergnes@mines-paristech.fr)  
45  
46  
47  
48  
49  
50  
51  
52  
53  
54  
55  
56  
57  
58  
59  
60

## ACKNOWLEDGEMENTS

This work was supported by the INTERREG project COMPOSENS, funded by the European FEDER Program, the Wallonie (Belgium), the “Grand Est” Region and the “Ardennes” department (France). A part of this work was also supported by the “Grand Est” Region and the European FEDER Program within the frame of COFILI project (D2015050245). The authors also thank the Nano'Mat platform funded by the “Grand Est” Region, the DDRT Grand Est and the European FEDER Program, and Miguel Pernes and Alain Lemaitre (both from FARE) for their support during twin-screw extrusion.

## ABSTRACT

In a series of previous papers, models describing the breakage of lignocellulose fibers during melt mixing process were established and applied to predict fiber size changes when compounding composites in a twin-screw extruder. Different types of fibers were studied (flax, hemp, sisal, etc.), but always with the same matrix, namely polypropylene (PP) compatibilized with PP grafted with maleic anhydride (PP-g-MA). In the present study, the influence of the matrix was characterized, by comparing the results obtained with non-polar PP and polar poly(butylene succinate) (PBS) of similar viscosity. For flax and hemp fibers, morphology changes (in length and diameter) were characterized along the screws under various processing conditions (screw speed and feed rate). Whatever the conditions, breakage was more important with the PBS matrix. Moreover, the rheological properties of the composites were also different, indicating specific interactions between fibers and matrices. Atomic Force Microscopy was used to measure the adhesion between the different matrices and AFM levers functionalized with nanocrystalline cellulose. The results confirmed a better interaction between the nanocrystalline cellulose and the PBS matrix compared to the PP one.

**Keywords:** lignocellulosic fibers, breakage, twin-screw extrusion, rheology, interactions

## 1. INTRODUCTION

The use of lignocellulosic fibers to reinforce thermoplastic polymers has now become common and concrete industrial applications can be found, especially in the automotive industry. For a general presentation of vegetal fibers-based composites, we refer the reader to recent reviews on this topic [1-5]. Thermoplastic composites reinforced with short lignocellulosic fibers are usually prepared by twin-screw extrusion, because of the flexibility and the great mixing capacity of this process [6]. However, the severe flow conditions into the extruder result in fiber degradation, i.e. a decrease in diameter ( $D$ ), due to the separation of bundles into individual fibers, and also in length ( $L$ ), due to the breakage of bundles and single fibers [7-10]. The mechanical properties of the composite being, among other parameters, controlled by the length and the aspect ratio (length/diameter,  $L/D$ ) of the fibers, it is important to understand the mechanisms of evolution of the fiber dimensions during the extrusion process. This would allow to optimise the processing conditions (screw profile, screw speed, feed rate, and barrel temperatures) to limit fiber degradation and promote bundle separation rather than length reduction.

In a previous series of papers [11-13], a systematic study of the fiber breakage mechanisms during compounding has been developed. First, qualitative rheo-optical observations of fiber breakage mechanisms have been presented [11]. Then, quantitative laws describing changes in fiber dimensions during mixing with a polypropylene matrix have been proposed [12]. Finally, dimensional changes of various types of fibers during the twin-screw extrusion process have been analyzed [13]. In all these studies, the matrix was a polypropylene (PP), compatibilized with a polypropylene grafted with maleic anhydride (PP-g-MA). It has been shown that the breakage mechanisms and the kinetics depend on the type of fiber (botanical origin, which determines the chemical composition and the morphology), its initial dimensions (the long fibers break more quickly) and its environment (water content,

1  
2  
3 temperature) [10-13]. In the present work, our intention is to highlight the role of the polarity  
4 of the matrix on the breakage mechanisms. Therefore, in addition to the non-polar PP,  
5 poly(butylene succinate) (PBS) was selected. PBS is an aliphatic thermoplastic polyester. Due  
6 to its biodegradability, PBS has already been used as a matrix for composites prepared with  
7 various types of fibers, for example abaca [14], hemp [15], coir [16], kenaf [17], sisal [18,  
8 19], curaua [19], sugar cane [20]. In the present case, it was chosen as a polar matrix, and flax  
9 and hemp fibers were selected because their breakage mechanisms are well known [11-13].

10  
11 The influence of the matrix on the properties of natural fiber-based composites has been  
12 studied by different authors. For example, Bourmaud et al. [21] compared the mechanical  
13 properties of flax-based composites made with PP, PBS and PLA, but without information on  
14 the respective viscosities of the matrices. Mano et al. [22] measured fiber dimensions before  
15 and after compounding for PP and PE/curaua composites, but again the viscosity curves were  
16 not presented. Teuber et al. [23] performed similar experiments, with wood particles and  
17 polyethylene (PE) and PP of various melt flow index (MFI). They observed higher  
18 degradation (particle size reduction) when the MFI was lower (and thus the viscosity higher),  
19 but a direct comparison between PE and PP was not possible because the MFI were measured  
20 under different conditions. Peltola et al. [24] compared wood fiber-based PLA and PP  
21 composites. They reported a greater reduction in fiber length for PLA, due to its higher  
22 viscosity (about twice that of PP). PP and PLA composites reinforced with abaca have also  
23 been studied by Jaszkievicz et al. [25] but the lack of viscosity data does not allow to draw  
24 clear conclusions. Hristov and Vlachopoulos [26] studied the flow behavior of wood flour/PE  
25 composites prepared with PE of different melt index and different molecular weight  
26 distribution. They reported a larger relative increase of viscosity for the composites prepared  
27 with the low molecular weight matrix and attributed this result to a better wetting of the fibers  
28 by the low viscosity product. Similarly, at constant fiber loading, they observed a higher  
29  
30  
31  
32  
33  
34  
35  
36  
37  
38  
39  
40  
41  
42  
43  
44  
45  
46  
47  
48  
49  
50  
51  
52  
53  
54  
55  
56  
57  
58  
59  
60

1  
2  
3 viscosity when adding a coupling agent, which was explained by a stronger fiber-matrix  
4 interaction. To our knowledge, only the paper of Lee et al. [27] presented a direct comparison  
5 between PP and PBS matrices for kenaf-based composites. PP and PBS had comparable  
6 viscosities (MFI of 21 and 25, respectively), but the composites were prepared under different  
7 conditions. Anyway, the reduction in fiber length was greater with PBS, despite the screw  
8 speed was lower (50 rpm instead of 100 rpm for PP). Moreover, by adding 30% kenaf fibers,  
9 the flexural modulus was increased by 65% for PP compatibilized with PP-g-MA, and by  
10 116% for the PBS. These results tend to show that, in addition to the level of viscosity, the  
11 affinity between the fiber and the matrix plays a role in the breakage mechanisms of the fibers  
12 and the resulting properties of the composites.  
13  
14  
15  
16  
17  
18  
19  
20  
21  
22  
23  
24  
25

26 In recent years, atomic force microscopy (AFM) has proven to be a relevant technique for  
27 investigating the interaction between matrix and fibers [28-30]. These studies used colloidal  
28 probe microscopy to directly measure adhesion forces between matrix and plant fibers or  
29 model polysaccharide films, using PLA microbeads attached to the AFM tips. Microbeads of  
30 cellulose triacetate have also been used to mimic cellulosic fibers [31]. The main drawback of  
31 this approach is the necessity to know with a nanometer accuracy the indentation depth of the  
32 microsphere on the analyzed surface. In addition, the asperity of the cellulose microspheres  
33 can impact the contact area between the two surfaces. Moreover, the microbeads used are  
34 based on chemically modified cellulose which could interfere in the spectroscopy force  
35 measurements. Therefore, in the present study, single molecule force microscopy (SFMS) was  
36 used to address the intermolecular adhesion forces between the cellulose functionalized AFM  
37 tip-less levers and the polymer surface. Based on a previously developed methodology [32],  
38 AFM tipless levers were functionalized with nanocrystalline cellulose to mimic the high  
39 cellulose content in flax and hemp fibers. Then, the adhesion forces were measured on smooth  
40 surfaces of the different polymer matrices. With this alternative approach, all the  
41  
42  
43  
44  
45  
46  
47  
48  
49  
50  
51  
52  
53  
54  
55  
56  
57  
58  
59  
60



1  
2  
3 Figure 2, was very close to the one used in our previous study [13]. A left-handed element  
4 was located in zone 3 to ensure the melting of the polymer matrix and two blocks of four  
5 kneading discs were designed to disperse the fibers. The first one was staggered at 90°, while  
6  
7  
8  
9  
10 the second one was staggered at -60°.

11  
12 The matrix (pre-blend of PP and PP-g-MA pellets or PBS pellets) was introduced in zone 1,  
13  
14 melted in zone 3 and the fibers were then added in zone 4. Experiments were performed at  
15  
16  
17 two flow rates (3 and 6 kg/h) and two screw speeds (100 and 200 rpm). The barrel  
18  
19  
20 temperature was kept constant, at 180°C for PP and 140°C for PBS.

21  
22 Samples were collected for further analyses, not only at the die exit but also along the screws,  
23  
24 following a “dead-stop” procedure: after reaching steady state conditions, the feeding and  
25  
26  
27 screw rotation were suddenly stopped and the barrel was cooled down and extracted. Samples  
28  
29  
30 were taken at the locations indicated in Figure 2.

### 31 **2.3 Characterization of fiber dimensions**

32  
33 The dimensions of the fibers were obtained according to the methodology of Di Giuseppe et  
34  
35  
36 al. [35], after dissolving the matrix, acquiring images with a high resolution scanner (Epson  
37  
38  
39 Perfection® V550) and analyzing these images with the ImageJ software. The dissolution was  
40  
41  
42 carried out in xylene for PP-based composites and in dichloromethane for PBS ones. Size  
43  
44  
45 distributions in length ( $L$ ), diameter ( $D$ ) and aspect ratio ( $L/D$ ) were then obtained, and, from  
46  
47  
48 these distributions, average values were calculated. In what follows, we focus on the weight  
49  
50  
51 average values.

### 52 **2.4 Rheological behavior**

53  
54 The viscoelastic properties of the composites were measured in small amplitude oscillatory  
55  
56  
57 shear. An Ares rheometer (TA Instruments, New Castle, DE, USA) was used. The parallel  
58  
59  
60 plate geometry had a diameter of 25 mm and a gap of 2 mm. The linear domain at 100 rad/s

was first defined using strain sweeps. Then, frequency sweeps were performed at three temperatures to measure the rheological behavior of the composites.

## 2.5 Process modeling and breakage laws

The flow parameters along the screws were calculated using the Ludovic<sup>®</sup> software developed about twenty years ago by one of us [36] and marketed by SCC company (Sciences Computers Consultants, Saint Etienne, France). It is a global model based on continuum mechanics, which simulates the whole extrusion process, from the introduction of solid polymer pellets in the hopper to the die exit. It has been used successfully to calculate the breakage of glass fibers during compounding operations [37-39] and, more recently, has also been applied to the breakage of lignocellulosic fibers, by using the evolution laws established in our previous work [13, 40]. For example, the weight average fiber length  $L_w$  can be calculated as:

$$L_w = L_\infty + (L_0 - L_\infty) \exp(-k_L \Gamma) \quad (1)$$

$L_0$  is the initial fiber length,  $L_\infty$  is its ultimate value,  $\Gamma$  is the cumulative strain and  $k_L$  is a kinetic constant. Similarly, the changes in weight average diameter can be expressed as:

$$D_w = D_\infty + (D_0 - D_\infty) \exp(-k_D \Gamma) \quad (2)$$

in which  $D_0$  is the initial fiber diameter,  $D_\infty$  is its ultimate value, and  $k_D$  is a kinetic constant.

The local strain is defined as the product of the local shear rate by the local residence time. It is then cumulated from the introduction of the fibers to the considered sampling point. Since the strain cannot be measured directly during the extrusion process, the Ludovic<sup>®</sup> software was used to estimate this parameter which controls the changes in the fiber dimensions.

## 2.6 Mechanical properties

Following the norm ISO 527-2 5A, dumbbell-shaped specimens were prepared by injection molding. A Babyplast<sup>®</sup> 6/10P injection molding machine (Molteno, Italy) was used. As

1  
2  
3 shown previously [41], this processing step has a small impact on the dimensions of the  
4  
5 fibers. Main mechanical properties (Young's modulus, stress and elongation at break) were  
6  
7 evaluated in uniaxial extension. A TEST 108 universal testing machine (TEST, Erkrath,  
8  
9 Germany) was used. It was controlled by the Testwinner 922 program. Test conditions were  
10  
11 as follows: 2 kN load cell, speed of 10 mm/min, and 10 replicates to test the reproducibility.  
12  
13  
14

## 15 **2.7 Measurements of fiber/matrix adhesion force at nanoscale**

16  
17 To investigate the adhesion forces between the fibers and the different matrices, Single  
18  
19 Molecule Force Spectroscopy (SMFS) measurements were performed using a Multimode-8  
20  
21 Atomic Force Microscope (Santa Barbara, CA, USA). Tip-less AFM levers were  
22  
23 functionalized with nanocrystalline cellulose using a protocol described elsewhere to  
24  
25 accurately control the cellulose nanorods density on the lever [32]. Briefly, a Langmuir-  
26  
27 Blodgett procedure was used to deposit the nanocrystalline cellulose extracted from bleached  
28  
29 ramie fibers on a tip-less AFM lever (NP-O levers from Bruker Nano, Santa Barbara, USA).  
30  
31 By controlling the surface pressure during the transfer, it is possible to obtain a known density  
32  
33 of cellulose nanorods on the AFM lever. **To sum up, the functionalized tip-less AFM lever  
34  
35 with CNCs was mounted on a sample holder and AFM images were acquired on the AFM  
36  
37 lever surface grafted with CNCs. Then the different images were treated and analyzed to  
38  
39 determine the surface of the CNCs rods observed in the different areas scanned. Using AFM  
40  
41 is the most suitable way to determine this coverage. Indeed, due to the size of the CNCs, their  
42  
43 organic and non-conductive nature, SEM is not as precise as AFM. A charging effect is  
44  
45 occurring under vacuum (or a loss of resolution if working in a pressure-controlled SEM),  
46  
47 which makes the SEM images less accurate as the AFM ones.** As the contact area between the  
48  
49 AFM lever and the surface under study is of paramount importance during SMFS  
50  
51 measurements, the nanocrystalline cellulose coverage of 56% was chosen to ensure  
52  
53 appropriate interactions between the cellulose nanorods and the different surfaces. The force  
54  
55  
56  
57  
58  
59  
60

1  
2  
3 measurements were then performed between functionalized levers having a similar  
4 nanocrystalline cellulose coverage and PP, PP-g-MA and PBS surfaces. Smooth polymer  
5 surfaces were prepared as 20  $\mu\text{m}$  thick sections obtained from polymer extrudates using a  
6 microtome equipped with a tungsten knife (Microm Microtech, France). All AFM  
7 measurements were carried out under controlled temperature and relative humidity (RH)  
8 conditions in a sealed chamber. A constant temperature of 25°C was maintained thanks to a  
9 Peltier holder and the RH was kept at 45% using a Wetsys humidity generator (Setaram  
10 Instrumentation).

11  
12  
13  
14  
15  
16  
17  
18  
19  
20  
21 As the goal of this part was to measure the adhesion forces between a functionalized tip and a  
22 given substrate, we used the most proper and accurate technique which is Force-Volume  
23 measurements, as it is performed in other similar publications.

24  
25  
26  
27  
28  
29 As for the adhesion measurements, using the Peak-Force Tapping mode is less reliable as the  
30 Force-Volume measurements: indeed, first, the functionalized tip will displace along the  
31 sample and then will lose its integrity after a few images, and second, the calibration of the  
32 mode to get quantitative data for the Young's modulus cartography of the deformation will be  
33 very imprecise as it necessitates a perfect characterization of the tip curvature radius which is  
34 not possible for the tip-less functionalized tip. Thus, we think that the more accurate and  
35 reliable information will come from Force-Volume measurements which is the more used  
36 mode to perform adhesion measurements. Therefore, Force-Volume (F-V) measurements  
37 were made for scan size areas of 5  $\mu\text{m}$  x 5  $\mu\text{m}$  with a resolution of 48 pixels per line, 200 nN/s  
38 as the loading rate, 0 seconds as the retract delay. For each condition, the average values of  
39 the adhesion force were obtained after analysis of a representative area of each sample,  
40 leading to 2304 force curves. Histograms of the adhesion data were fitted by a Gaussian  
41 distribution.

42  
43  
44  
45  
46  
47  
48  
49  
50  
51  
52  
53  
54  
55  
56  
57  
58  
59  
60

To obtain reliable adhesion measurements, a limited surface roughness is required to ensure a constant contact area. Thus, prior to the SMFS measurements, conventional AFM experiments were performed to locate an appropriate area on the PP, PP-g-MA and PBS surfaces. Topographical images were acquired in the Peak Force Tapping Mode using ScanAsyst air probes (Bruker Nano, Santa Barbara, USA) with a nominal tip radius of 2 nm, a nominal spring constant of 0.4 N/m and a nominal resonant frequency of 70 kHz. Images of 512 x 512 pixels were acquired using a frequency of 1 kHz and a scan rate of 0.4 Hz. The raw images were analyzed using Nanoscope V and Gwyddion [42] software. To characterize the surface roughness, the arithmetic average roughness parameter ( $R_a$ ) was used [43]. Average  $R_a$  parameters were measured using at least three representative AFM images from different scan areas of the PP, PP-g-MA and PBS surfaces. In addition to these preliminary images, the topography of the functionalized levers and the different surfaces was systematically recorded before and after the F-V acquisition to ensure that no artefact or interferential events such as significant nanocrystalline cellulose detachment occurred during the adhesion measurements. Reference experiments (not shown here) were also performed on the different surfaces with a non-functionalized lever to ensure that the adhesion forces measured with the functionalized lever were specific.

### 3. RESULTS AND DISCUSSION

#### 3.1 Morphological changes along the screws

Figure 3 shows an example of change in fiber length along the screws for the flax-based composites at 3 kg/h and 100 rpm. As expected, the fibers undergo a significant reduction in length, but it is evident that this degradation is more pronounced with the PBS matrix. The same observations can be made for fiber diameters (Figure 4). While it remains quite constant with PP/PP-g-MA, a slight decrease is observed with PBS. Similar results were obtained for the other processing conditions and the hemp fibers (not shown). In all cases, the

1  
2  
3 morphological evolutions were greater with the PBS matrix. It has been shown previously  
4 [13] that, for different values of screw speed and feed rate, a mastercurve was obtained when  
5 plotting the weight average length (or diameter) as a function of the calculated cumulative  
6 strain (see Eqs. (1) and (2)). For each matrix and each fiber, four processing conditions were  
7 tested, and, for each condition, five samples were collected along the screws. An example of  
8 results for the flax-based composites is shown in Figure 5. For a fixed value of the strain, the  
9 fiber length is always shorter with the PBS matrix, even though its viscosity is slightly lower  
10 than that of PP/PP-g-MA. This result is also valid for the fiber diameter (Figure 6). It is also  
11 important to emphasize that the evolution laws proposed previously [13] remain valid for the  
12 various matrices and fibers. However, diameters are more difficult to evaluate than lengths.  
13 Therefore, the dispersion between the various samples corresponding to different processing  
14 conditions and different locations along the screws is significant and the fit by a unique  
15 exponential function is less accurate, especially for PP/PP-g-MA. The kinetic constants are  
16 indicated in Table 2. For PP-based composites, the values are close to those determined in our  
17 previous work [13]. The slight differences come from the fact that the fibers used were  
18 different. The values of  $k_L$  and  $k_D$  confirm that the breakage kinetics are faster with PBS.  
19 Starting from longer fibers (4 mm for flax, 2 mm for hemp), the kinetics are also faster, but  
20 the final dimensions are comparable: about 1 mm for PP and 0.5 mm for PBS. PP-based  
21 composites have also larger final diameters (50-70  $\mu\text{m}$ , compared to 35-40  $\mu\text{m}$  for PBS) and  
22 higher aspect ratio (10-14, compared to 6 for PBS).

23  
24  
25  
26  
27  
28  
29  
30  
31  
32  
33  
34  
35  
36  
37  
38  
39  
40  
41  
42  
43  
44  
45  
46  
47  
48  
49 To summarize, whatever the fiber and the processing conditions, fiber breakage (i.e. reduction  
50 in length and diameter) is always more significant with the PBS matrix, despite a slightly  
51 lower viscosity compared to PP/PP-g-MA. This can be only explained by stronger  
52 interactions between the lignocellulosic fibers and the PBS matrix, even though PP-g-MA has  
53 been used as a compatibilizer for PP.  
54  
55  
56  
57  
58  
59  
60

### 3.2 Rheological behavior

Rheological measurements in small amplitude oscillatory shear were performed in the linear domain on samples collected at the die exit, extruded at 6 kg/h and 100 rpm. The experiments were performed at three temperatures (180°C, 190°C, 200°C and 140°C, 160°C, 180°C for PP/PP-g-MA and PBS, respectively) and mastercurves at 180°C were obtained by time/temperature superposition. Figure 7 compares the complex viscosity curves of the PP-based composites with that of the matrix. The composites obviously have much higher viscosities, but the behavior differs according to the fiber type: when the hemp exhibits a Carreau-Yasuda behavior, similar to that of the matrix, the flax presents an apparent yield stress at low frequency. The presence of a yield stress in lignocellulosic fiber composites above 20-30wt% has been reported by many authors [44-47]. It is due to the interactions between the fibers, which are more significant for flax because of higher aspect ratio (23, instead of 15 for hemp). Similar tendencies are observed for PBS-based composites (Figure 8), except that flax is now more viscous than hemp. It means that the interactions between PBS, hemp and flax are different from those between PP/PP-g-MA, hemp and flax. This is clearly demonstrated if we now compare the same fiber with both matrices. For hemp, PP- and PBS-based composites have similar viscosities, despite the fiber aspect ratios are higher for PP (15 instead of 5) and the viscosity of the PBS matrix is lower (Figure 9). This shows a higher affinity of hemp with PBS. These results are confirmed by the flax-based composites (Figure 10). The viscosity of flax/PBS is now about three times that of flax/PP/PP-g-MA, when the aspect ratio is 23 for flax/PP/PP-g-MA and 9 for flax/PBS. As for the fiber breakage, these results can only be explained by the different interactions in the molten state between fibers and matrices. Li and Wolcott [48] have already noticed an increase in viscosity in the presence of maleated polymer in the case of wood flour/PE composites, attributed to enhanced interactions between wood and PE.

In all cases, the complex viscosity of the matrices and the composites can be nicely fitted by a Carreau-Yasuda law, eventually with a yield stress:

$$\eta^*(\omega) = \frac{\sigma_0}{\omega} + \eta_0 a_T \left[ 1 + (\lambda a_T \omega)^a \right]^{\frac{n-1}{a}} \quad (3)$$

$\omega$  is the angular frequency,  $\sigma_0$  is the melt yield stress,  $\eta_0$  is the viscosity of the Newtonian plateau,  $\lambda$  is a characteristic time,  $n$  is the power law exponent, and  $a$  is the Yasuda parameter.

$a_T$  is the temperature shift factor which is defined by an Arrhenius law:

$$a_T = \exp \left[ \frac{E}{R} \left( \frac{1}{T} - \frac{1}{T_0} \right) \right] \quad (4)$$

$E$  is the activation energy,  $R$  is the gas constant, and  $T_0$  is the reference temperature.

The parameters of these laws for the different composites are provided in Table 3.

### 3.3 Mechanical properties

Measurements in uniaxial tension have been performed to check if the preferred interactions observed in the molten state are retained in the solid state. Figure 11a presents the relative Young's modulus (i.e. the Young's modulus of the composite divided by that of the matrix) for the various composites. It is clear that the mechanical reinforcement is much more efficient for PBS-based composites. For each matrix, the higher values measured for flax compared to hemp can be explained by the higher lengths and aspect ratios measured after compounding. In contrast, the stress at break is quite unchanged (Figure 11b). As expected, the elongation at break is largely reduced for composites (Figure 11c). For these two last parameters, there is practically no difference between flax and hemp, and between PP and PBS. The orders of magnitude of our results are globally in good agreement with those obtained by Bourmaud et al. [21] or Baiardo et al. [49] on flax/PBS composites.

### 3.4 Fiber/matrix adhesion forces

To investigate the intermolecular interactions between the cellulosic fiber and the polymer matrix, Single Molecule Force Spectroscopy (SMFS) measurements were carried out by using AFM levers functionalized with nanocrystalline cellulose. In such experiments, force measurements are carried out to determine adhesion between the probe and a selected surface. In this study, the probe (a flat cantilever) was functionalized with nanocrystalline cellulose as it is the main constituent of hemp and flax fibers. The aspect ratio of the nanocrystalline cellulose is 30, being in the same range as the aspect ratio of hemp and flax fibers (Table 1). As the interactions between two surfaces strongly depends on their load contact area [50], a high coverage of the probes with nanocrystalline cellulose ( $55.8 \pm 2.6\%$ ) [32] and a surface of low roughness for the matrices (PP, PP/PP-g-MA and PBS) were chosen to ensure the comparison between each surface. Thus, areas of similar roughness were selected for SMFS measurements to ensure that the interaction between the nanocrystalline cellulose and the section of interest was determined over similar contact areas (roughness parameter  $R_a$  of PP, PP/PP-g-MA and PBS surfaces was 53.8 nm, 51.8 nm and 49.1 nm, respectively. See Figure 12). The adhesion force mapping acquired for scan sizes of  $5 \mu\text{m} \times 5 \mu\text{m}$  clearly exhibit homogenous values of the adhesion for each sections (Figure 12). Representative force curves derived from adhesion mapping images are shown in Figure 13. PBS shows to be the matrix which presents significant higher interaction with nanocrystalline cellulose, followed by PP/PP-g-MA and PP matrices. As expected, the interaction between PP/PP-g-MA and cellulose nanorods is slightly greater than that of pure PP. Quantitative average values of adhesion forces between nanocrystalline cellulose and each surface were extracted from adhesion mapping (Figure 14). The interaction is greater between the nanocrystalline cellulose and PBS ( $16.3 \pm 2.1 \text{ nN}$ ) compared to PP/PP-g-MA ( $10.3 \pm 2.9 \text{ nN}$ ) or PP ( $8.0 \pm 1.4 \text{ nN}$ ). The differences between the measured adhesion values are fully consistent with the

1  
2  
3 results observed at macroscale, showing the importance of the interaction between the fibers  
4 and the matrix. The adhesion values obtained at the nanoscale by SMFS confirm the effect of  
5 the PP-g-MA as a compatibilizer, but also the differences in behavior between PBS and PP  
6 matrices. Such observations at molecular scale could be explained by the fact that the  
7 intermolecular interactions between the nanocrystalline cellulose and the various matrices are  
8 strongly dependent on hydrogen bonding. The nanocrystalline cellulose consists of rods  
9 whose lateral faces are fully covered by hydroxyl moieties. These hydroxyl groups are  
10 hydrogen bond donors and may tend to form hydrogen bonds with the ester groups of PBS  
11 and the maleic anhydride groups of PP-g-MA. There are more ester groups in PBS than  
12 maleic anhydride moieties in PP/PP-g-MA which explains the difference of interaction with  
13 nanocrystalline cellulose. Finally, PP is a hydrophobic and non-polar matrix. The absence of  
14 hydrogen bonds and electrostatic interactions makes the complex nanocrystalline cellulose/PP  
15 with the weakest interaction compared to the rest of studied composites.  
16  
17  
18  
19  
20  
21  
22  
23  
24  
25  
26  
27  
28  
29  
30  
31  
32  
33

#### 34 4. CONCLUSION

35  
36 In this paper, the role of the polarity of the matrix on the breakage mechanism and the  
37 rheological behavior of lignocellulosic fiber based-composites was investigated. By extruding  
38 under the same conditions flax and hemp-based composites with a non-polar and a polar  
39 matrix of similar viscosity, it has been shown that breakage (i.e. reduction in length and  
40 diameter of the fibers and bundles) is more important with the polar matrix. Moreover, the  
41 complex viscosity of PBS-based composites is systematically higher than that of PP-based  
42 ones, even though the aspect ratios are smaller. Finally, the Young's modulus of PBS is much  
43 more improved by the presence of flax or hemp fibers than that of PP/PP-g-MA. All these  
44 results can be interpreted by a better affinity between the lignocellulosic fibers and the PBS  
45 matrix. To validate this assumption, the adhesion properties between nanocrystalline cellulose  
46  
47  
48  
49  
50  
51  
52  
53  
54  
55  
56  
57  
58  
59  
60

and various surfaces (PP, PP/PP-g-MA, PBS) were characterized by SMFS measurements. Higher adhesion forces were confirmed with PBS, followed by PP/PP-g-MA and finally PP.

## REFERENCES

- [1] J. Summerscales, N.P.J. Dissanayake, A.S. Virk, W. Hall, *Comp. Part A* **2010**, *41*, 1329.
- [2] O. Faruk, A.K. Bledzki, H.P. Fink, M. Sain M, *Macromol. Mat. Eng.* **2014**, *299*, 9.
- [3] P.H. Fernandes Pereira, M. de Freitas Rosa, M.O. Hilario Cioffi, K.C. Coelho de Carvalho Benini, A.C. Milanese, H.J.C. Voorwald, D.R. Mulinari, *Polimeros* **2015**, *25*, 9.
- [4] T. Gurunathan, S. Mohanty, S.K. Nayak, *Comp. Part A* **2015**, *77*, 1.
- [5] K.L. Pickering, M.G.A. Efendy, T.M. Le, TM. *Comp. Part A* **2016**, *83*, 98.
- [6] A. Gallos, G. Paës, F. Allais, J. Beaugrand, J. *RSC Adv.* **2017**, *7*, 34638.
- [7] H.L. Bos, J. Müssig, M.J.A. van den Oever, *Comp. Part A* **2006**, *37*, 1591.
- [8] N.M. Barkoula, S.K. Garkhail, T. Peijs, *J. Reinf. Plast. Comp.* **2010**, *29*, 1366.
- [9] A.R. Dickson, D. Even, J.M. Warnes, A. Fernyhough, *Comp. Part A* **2014**, *61*, 258.
- [10] M. Feldmann, H.P. Heim, J.C. Zarges, *Comp. Part A* **2016**, *83*, 113.
- [11] R. Castellani, E. Di Giuseppe, S. Dobosz, J. Beaugrand, F. Berzin, B. Vergnes, T. Budtova, *Comp. Part A* **2016**, *91*, 229.
- [12] E. Di Giuseppe, R. Castellani, T. Budtova, B. Vergnes, *Comp. Part A* **2017**, *95*, 31.
- [13] F. Berzin, J. Beaugrand, S. Dobosz, T. Budtova, B. Vergnes, *Comp. Part A* **2017**, *101*, 422.
- [14] M. Shibata, K. Ozawa, N. Teramoto, R. Yosomiya, H. Takeishi, *Macromol. Mat. Eng.* **2003**, *288*, 35.
- [15] B.N. Dash, M. Nakamura, S. Sahoo, M. Kotaki, A. Nakai, H. Hamada, *J. Biobased Mat. Bio.* **2008**, *2*, 273.
- [16] T.H. Nam, S. Ogihara, N.H. Tung, S. Kobayashi, *Comp. Part B* **2011**, *42*, 1648.

- 1  
2  
3 [17] M.Z.A. Thirmizir, Z.A.M. Ishak, R.M. Taib, S. Raim, S.M. Jani, SM. *J. Appl. Polym.*  
4  
5 *Sci.* **2011**, *122*, 3055.  
6  
7 [18] Y.H. Feng, Y.J. Li, B.P. Xu, D.W. Zhang, J.P. Qu, H.Z. He, *Comp. Part B* **2013**, *44*, 193.  
8  
9 [19] E. Frollini, N. Bartolucci, L. Sisti, A. Celli, *Indus. Crops Prod.* **2013**, *45*, 160-169.  
10  
11 [20] Z. Huang, L. Qian, Q. Yin, N. Yu, T. Liu, D. Tian, *Polym. Test.* **2018**, *66*, 319.  
12  
13 [21] A. Bourmaud, Y.M. Corre, C. Baley, *Indus. Crops Prod.* **2015**, *64*, 251.  
14  
15 [22] B. Mano, J.R. Araújo, M.A.S. Spinacé, M.A. De Paoli, *Comp. Sci. Tech.* **2010**, *70*, 29.  
16  
17 [23] L. Teuber, H. Militz, A. Krause, *J. Appl. Polym. Sci.* **2015**, *43231*, 1.  
18  
19 [24] H. Peltola, E. Pääkkönen, P. Jetsu, S. Heinemann, *Comp. Part A* **2014**, *61*, 13.  
20  
21 [25] A. Jaszkievicz, A. Meljon, A.K. Bledzki, M. Radwanski, *Comp. Part A* **2016**, *83*, 140.  
22  
23 [26] V. Hristov, J. Vlachopoulos, *Macromol. Mat. Eng.* **2007**, *292*, 608.  
24  
25 [27] J.M. Lee, Z.A.M. Ishak, R.M. Taib, T.T. Law, M.Z.A. Thirmizir, *J. Polym. Environ.*  
26  
27 **2013**, *21*, 293.  
28  
29 [28] M. Le Troëdec, A. Rachini, C. Peyratout, S. Rossignol, E. Max, O. Kaftan, A. Ferry, A.  
30  
31 Smith, *J. Colloid Interf. Sci.* **2011**, *356*, 303.  
32  
33 [29] G. Raj, E. Balnois, M.A. Helias, C. Baley, Y. Grohens, *J. Mater. Sci.* **2012**, *47*, 2175.  
34  
35 [30] J. Colson, T. Pettersson, S. Asaadi, H. Sixta, T. Nypelö, A. Mautner, J. Konnerth, *J.*  
36  
37 *Colloid Interf. Sci.* **2018**, *532*, 819.  
38  
39 [31] G. Raj, E. Balnois, C. Baley, Y. Grohens, *Colloids Surf. A* **2009**, *352*, 47.  
40  
41 [32] C. Marcuello, L. Foulon, B. Chabbert, M. Molinari, V. Aguié-Béghin, *Langmuir* **2018**,  
42  
43 *34*, 9376.  
44  
45 [33] J. Gassan, A.K. Bledski, *Comp. Part A* **1997**, *28*, 1001.  
46  
47 [34] N. Le Moigne, M. van den Oever, T. Budtova, *Comp. Part A* **2011**, *42*, 1542.  
48  
49 [35] E. Di Giuseppe, R. Castellani, S. Dobosz, J. Malvestio, F. Berzin, J. Beaugrand, C.  
50  
51 Delisée, B. Vergnes, T. Budtova, *Comp. Part A* **2016**, *90*, 320.  
52  
53  
54  
55  
56  
57  
58  
59  
60

- 1  
2  
3 [36] B. Vergnes, G. Della Valle, L. Delamare, *Polym. Eng. Sci.* **1998**, 38, 1781.  
4  
5 [37] F. Inceoglu, J. Ville, N. Ghamri, A. Durin, R. Valette, B. Vergnes, *Polym. Comp.* **2011**,  
6  
7 32, 1842.  
8  
9 [38] A. Durin, P. De Micheli, J. Ville, F. Inceoglu, R. Valette, B. Vergnes, *Compos. Part A*  
10  
11 **2013**, 48, 47.  
12  
13 [39] J. Ville, F. Inceoglu, N. Ghamri, J.L. Pradel, A. Durin, R. Valette, B. Vergnes, *Intern.*  
14  
15 *Polym. Proc.* **2013**, 28, 49.  
16  
17 [40] F. Berzin, B. Vergnes, J. Beaugrand, *Comp. Part A* **2014**, 59, 30.  
18  
19 [41] F. Berzin, T. Amornsakchai, A. Lemaitre, E. Di Giuseppe, B. Vergnes, *Polym. Comp.*  
20  
21 **2018**, 39, 3817.  
22  
23 [42] D. Nečas, P. Klapetek, *Central Europ. J. Phys.* **2012**, 10, 181.  
24  
25 [43] British Standards Institution. BS EN ISO 4287, BSI, London, UK**1998**.  
26  
27 [44] A. Abdennadher, M. Vincent, T. Budtova, *J. Rheol.* **2016**, 60, 191.  
28  
29 [45] N. Le Moigne, M. van den Oever, T. Budtova, *Polym. Eng. Sci.* **2013**, 43, 1.  
30  
31 [46] M. Le Baillif, K. Oksman, *J. Therm. Comp. Mat.* **2009**, 22, 115.  
32  
33 [47] F. Berzin, T. Amornsakchai, A. Lemaitre, R. Castellani, B. Vergnes, *Polym. Comp.* **2019**,  
34  
35 in press, DOI 10.1002/pc.25308.  
36  
37 [48] T.Q. Li, M.P. Wolcott, *Polym. Eng. Sci.* **2005**, 35, 549.  
38  
39 [49] M. Baiardo, E. Zini, M. Scandola, *Comp. Part A* **2004**, 35, 703.  
40  
41 [50] D.F. Parsons, R.B. Walsh, V.S. Craig, *J. Chem. Phys.* **2014**, 140, 164701.  
42  
43  
44  
45  
46  
47  
48  
49  
50  
51  
52  
53  
54  
55  
56  
57  
58  
59  
60

Fiber	Average length $L_w$ (mm)	Average diameter $D_w$ ( $\mu\text{m}$ )	Average aspect ratio $(L/D)_w$ (-)	Hemicellulose (%)	Cellulose (%)	Lignin (%)
Flax	$3.88 \pm 0.05$	$70 \pm 5$	$43 \pm 4$	11.2	74.1	5.7
Hemp	$2.14 \pm 0.15$	$82 \pm 12$	$18 \pm 1$	11.2	76.9	5.1

Table 1. Average values of length, diameter and aspect ratio of the original fibers, and composition.

Kinetic constant	PP/PP-g-MA /Flax	PBS/Flax	PP/PP-g-MA /Hemp	PBS/Hemp
$k_L$	$1.5 \cdot 10^{-3}$	$1.8 \cdot 10^{-3}$	$0.8 \cdot 10^{-3}$	$2.0 \cdot 10^{-3}$
$k_D$	$0.7 \cdot 10^{-3}$	$2.5 \cdot 10^{-3}$	$1.0 \cdot 10^{-3}$	$3.0 \cdot 10^{-3}$

Table 2. Values of kinetic constants for the breakage laws of the various composites.

Material	$\sigma_0$ (Pa)	$\eta_0$ (Pa.s)	$\lambda$ (s)	$n$ (-)	$a$ (-)	$E$ (kJ/mol)
PP/PP-g-MA	0	4 500	0.65	0.46	1	39.9
Flax/PP/PP-g-MA	3000	19 000	1.90	0.48	0.40	57.2
Hemp/PP/PP-g-MA	0	87 400	8.05	0.42	0.43	74.3
PBS	0	3100	0.60	0.51	0.70	35.8
Flax/PBS	20 000	22 000	1.00	0.48	0.70	48.2
Hemp/PBS	2500	25 000	2.00	0.44	0.50	68.6

Table 3. Parameters of the Carreau-Yasuda law with yield stress (for a reference temperature  $T_0 = 180^\circ\text{C}$ ).

**FIGURE CAPTIONS**

Figure 1. Complex viscosity curves of PP (with 2.5% PP-g-MA) and PBS at 180°C. Full lines are fits with the Carreau-Yasuda model.

Figure 2. Scheme of the laboratory scale twin-screw extruder (Leistritz ZSE 27). Restrictive zones are in grey. Arrows indicate sampling locations.

Figure 3. Changes in weight average fiber length along the screws for a fixed processing condition. Lines are just to guide the eyes.

Figure 4. Changes in weight average fiber diameter along the screws for a fixed processing condition. Lines are just to guide the eyes.

Figure 5. Changes in weight average fiber length as functions of the cumulative strain for various processing conditions. Full lines are fits with Eq. (1).

Figure 6. Changes in weight average fiber diameter as functions of the cumulative strain for various processing conditions. Full lines are fits with Eq. (2).

Figure 7. Complex viscosity curves of PP/PP-g-MA and PP-based composites at 180°C. Full lines are fits with a Carreau-Yasuda model.

Figure 8. Complex viscosity curves of PBS and PBS-based composites at 180°C. Full lines are fits with a Carreau-Yasuda model.

Figure 9. Complex viscosity curves of the two matrices and the corresponding hemp-based composites at 180°C. Full lines are fits with a Carreau-Yasuda model.

Figure 10. Complex viscosity curves of the two matrices and the corresponding flax-based composites at 180°C. Full lines are fits with a Carreau-Yasuda model.

Figure 11. Mechanical properties of the various composites. (a) Relative Young's modulus, (b) Stress at break, (c) Elongation at break. PP means PP/PP-g-MA.

Figure 12. Force spectroscopy experiments between nanocrystalline cellulose-functionalized AFM levers (coverage of nanocrystalline cellulose is  $55.8 \pm 2.6\%$ ). Topography channel

1  
2  
3 (a) and adhesion force map (b) regarding, from top to bottom, PP, PP/PP-g-MA and PBS  
4 surfaces. Scan size is 25  $\mu\text{m}^2$  for all sections. Temperature and RH are fixed at 25°C and  
5  
6  
7  
8 45%, respectively.  
9

10 Figure 13. Representative force-distance curve for nanocrystalline cellulose functionalized  
11  
12 AFM levers with PP, PP/PP-g-MA and PBS surfaces.  
13

14 Figure 14. Intermolecular adhesion forces between nanocrystalline cellulose functionalized  
15  
16 AFM levers with PP, PP/PP-g-MA and PBS at 25°C and 45% RH.  
17  
18  
19  
20  
21  
22  
23  
24  
25  
26  
27  
28  
29  
30  
31  
32  
33  
34  
35  
36  
37  
38  
39  
40  
41  
42  
43  
44  
45  
46  
47  
48  
49  
50  
51  
52  
53  
54  
55  
56  
57  
58  
59  
60

For Peer Review

Fiber	Average length $L_w$ (mm)	Average diameter $D_w$ ( $\mu\text{m}$ )	Average aspect ratio $(L/D)_w$ (-)	Hemicellulose (%)	Cellulose (%)	Lignin (%)
Flax	$3.88 \pm 0.05$	$70 \pm 5$	$43 \pm 4$	11.2	74.1	5.7
Hemp	$2.14 \pm 0.15$	$82 \pm 12$	$18 \pm 1$	11.2	76.9	5.1

Table 1. Average values of length, diameter and aspect ratio of the original fibers, and composition.

Kinetic constant	PP/PP-g-MA /Flax	PBS/Flax	PP/PP-g-MA /Hemp	PBS/Hemp
$k_L$	$1.5 \cdot 10^{-3}$	$1.8 \cdot 10^{-3}$	$0.8 \cdot 10^{-3}$	$2.0 \cdot 10^{-3}$
$k_D$	$0.7 \cdot 10^{-3}$	$2.5 \cdot 10^{-3}$	$1.0 \cdot 10^{-3}$	$3.0 \cdot 10^{-3}$

Table 2. Values of kinetic constants for the breakage laws of the various composites.

Material	$\sigma_0$ (Pa)	$\eta_0$ (Pa.s)	$\lambda$ (s)	$n$ (-)	$a$ (-)	$E$ (kJ/mol)
PP/PP-g-MA	0	4 500	0.65	0.46	1	39.9
Flax/PP/PP-g-MA	3000	19 000	1.90	0.48	0.40	57.2
Hemp/PP/PP-g-MA	0	87 400	8.05	0.42	0.43	74.3
PBS	0	3100	0.60	0.51	0.70	35.8
Flax/PBS	20 000	22 000	1.00	0.48	0.70	48.2
Hemp/PBS	2500	25 000	2.00	0.44	0.50	68.6

Table 3. Parameters of the Carreau-Yasuda law with yield stress (for a reference temperature  $T_0 = 180^\circ\text{C}$ ).

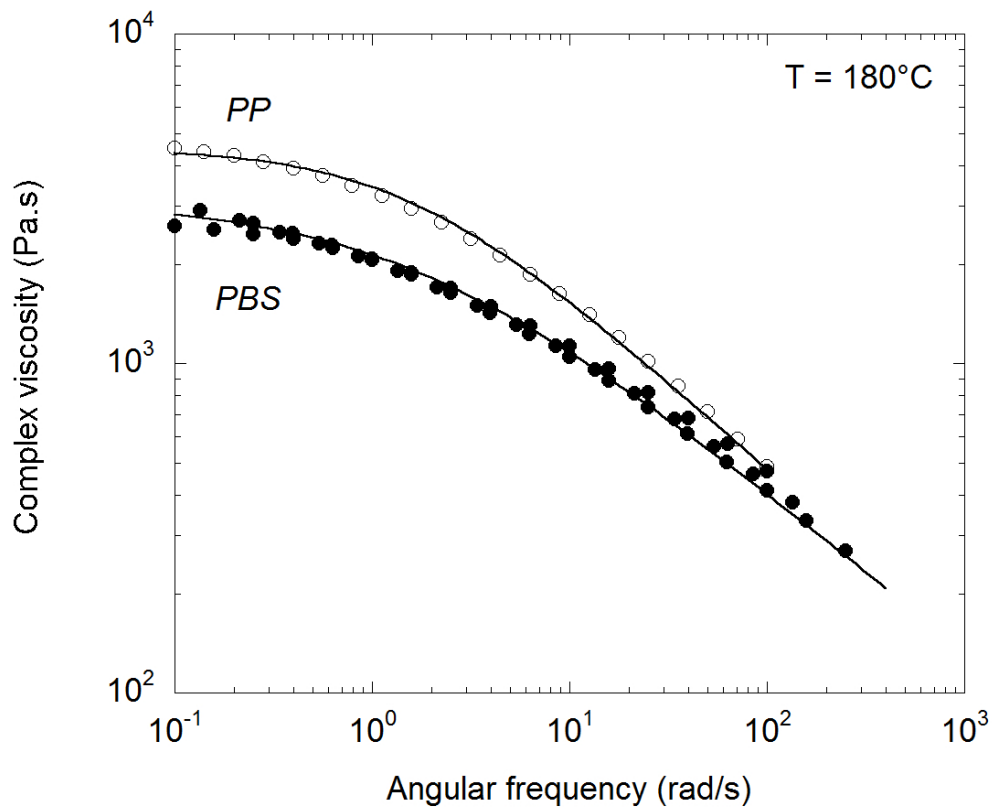


Figure 1. Complex viscosity curves of PP (with 2.5% PP-g-MA) and PBS at 180°C. Full lines are fits with the Carreau-Yasuda model.

1  
2  
3  
4  
5  
6  
7  
8  
9  
10  
11  
12  
13  
14  
15  
16  
17  
18  
19  
20  
21  
22  
23  
24  
25  
26  
27  
28  
29  
30  
31  
32  
33  
34  
35  
36  
37  
38  
39  
40  
41  
42  
43  
44  
45  
46  
47  
48  
49  
50  
51  
52  
53  
54  
55  
56  
57  
58  
59  
60

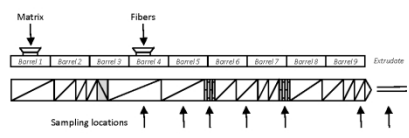


Fig 2

279x215mm (200 x 200 DPI)

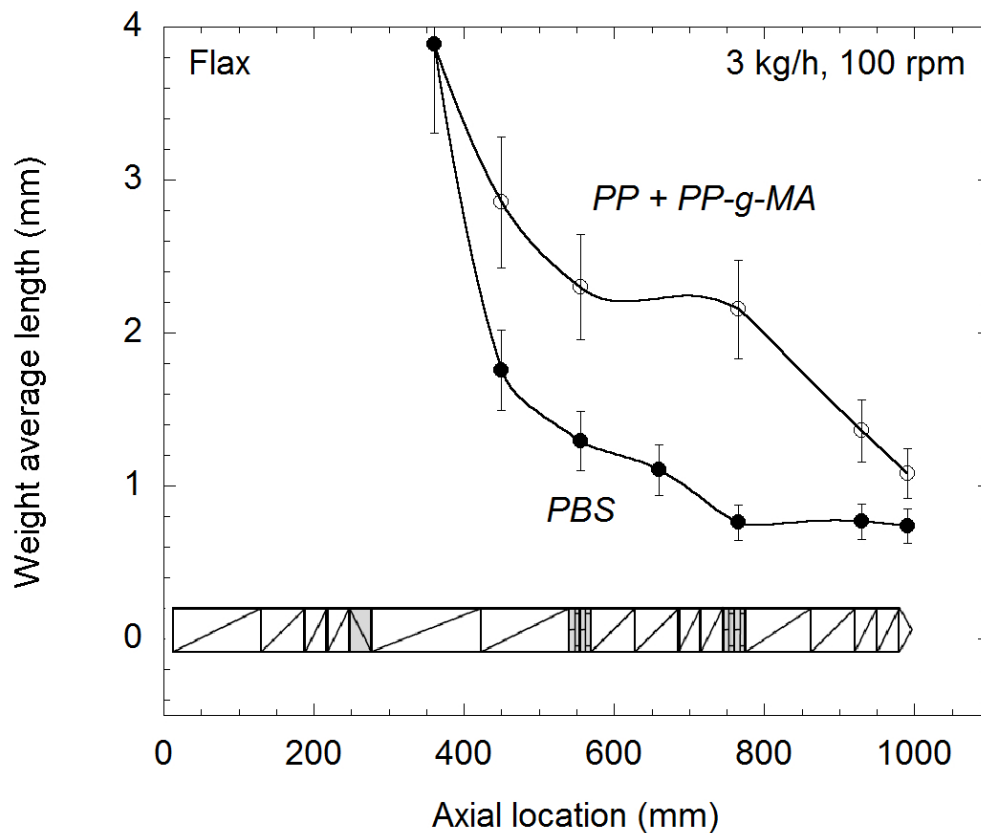


Figure 3. Changes in weight average fiber length along the screws for a fixed processing condition. Lines are just to guide the eyes.

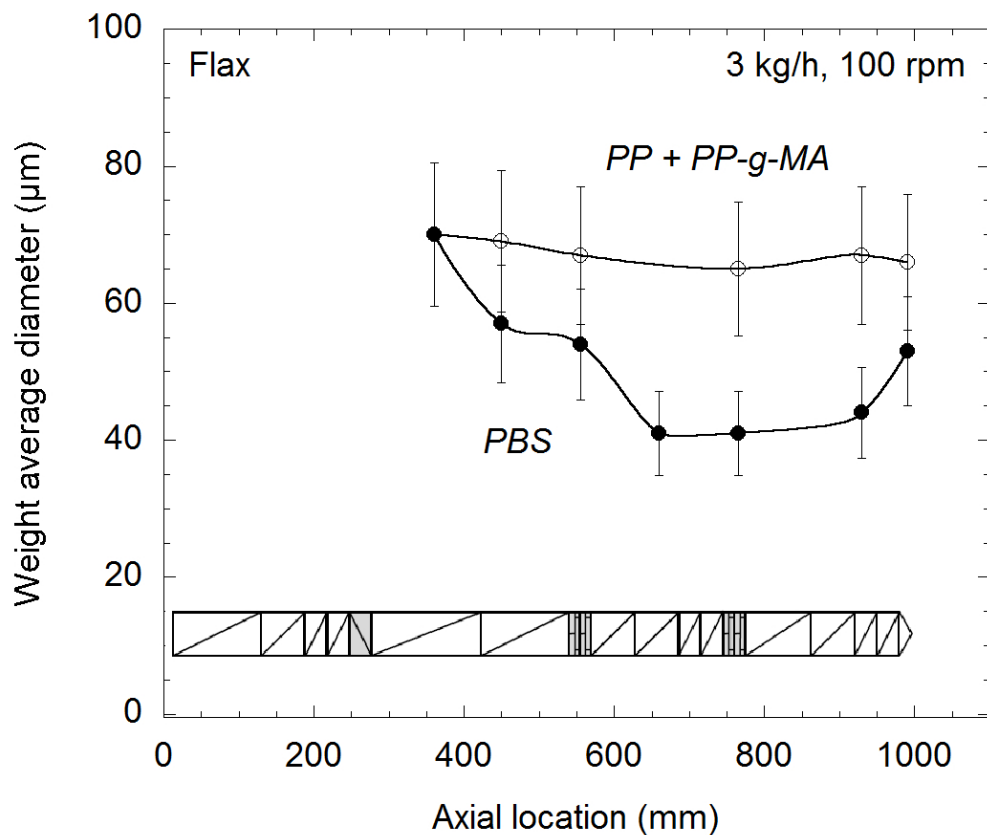


Figure 4. Changes in weight average fiber diameter along the screws for a fixed processing condition. Lines are just to guide the eyes.

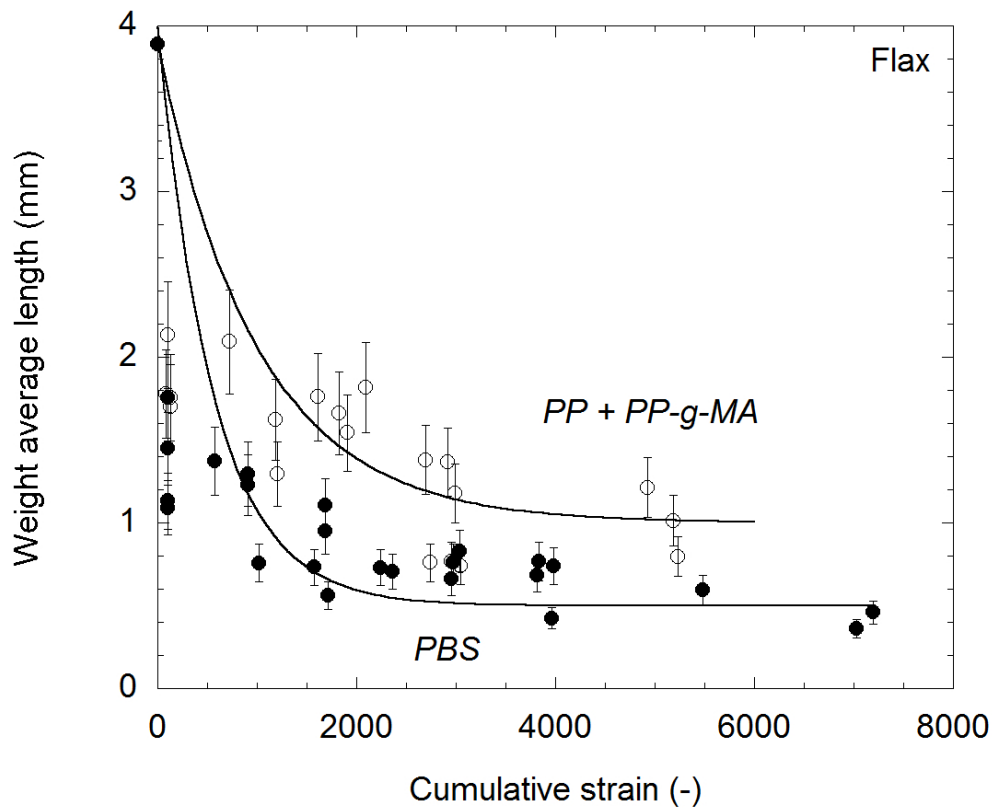


Figure 5. Changes in weight average fiber length as functions of the cumulative strain for various processing conditions. Full lines are fits with Eq. (1).

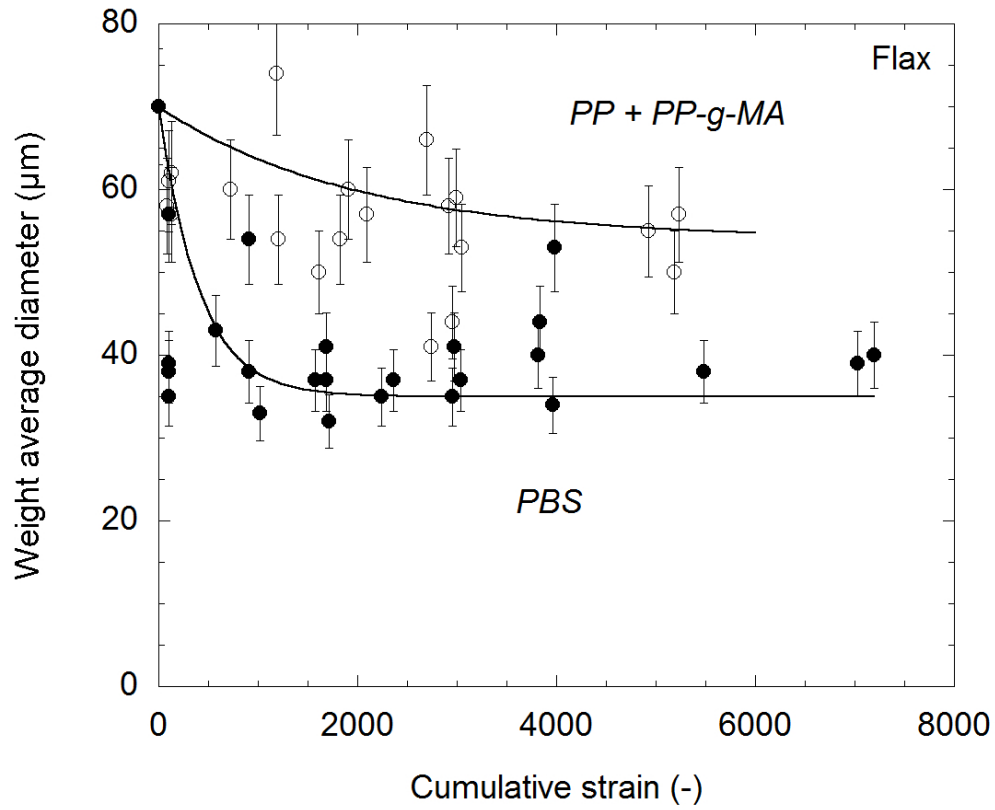


Figure 6. Changes in weight average fiber diameter as functions of the cumulative strain for various processing conditions. Full lines are fits with Eq. (2).

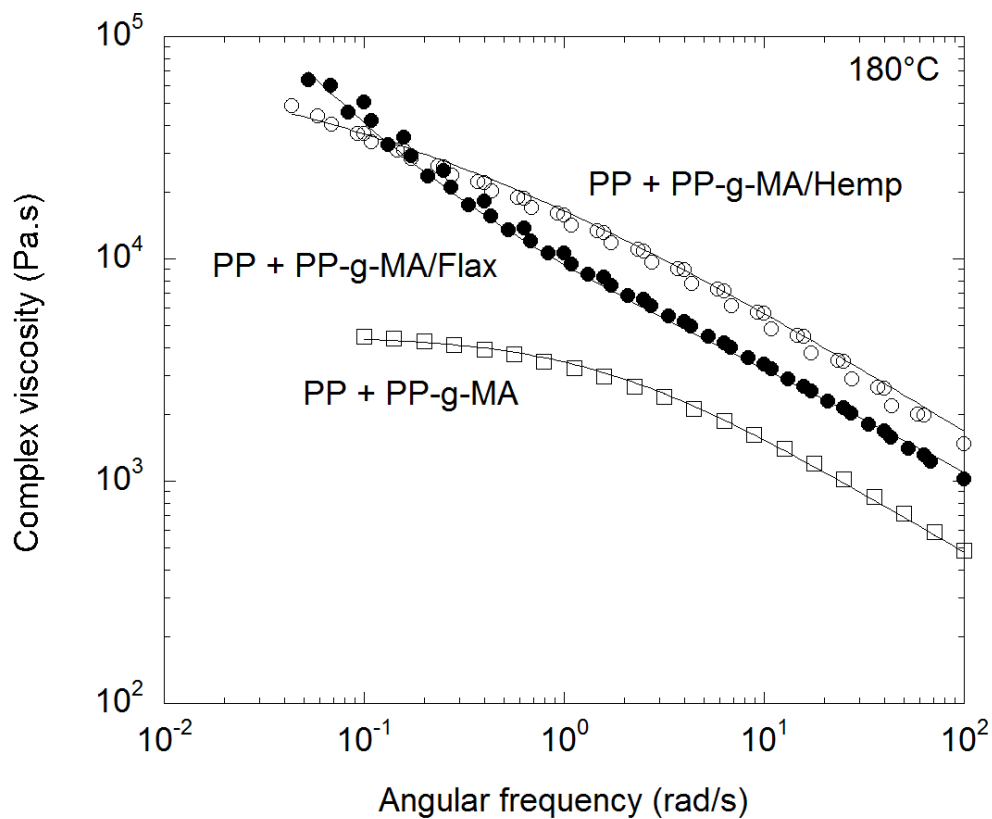


Figure 7. Complex viscosity curves of PP/PP-g-MA and PP-based composites at 180°C. Full lines are fits with a Carreau-Yasuda model.

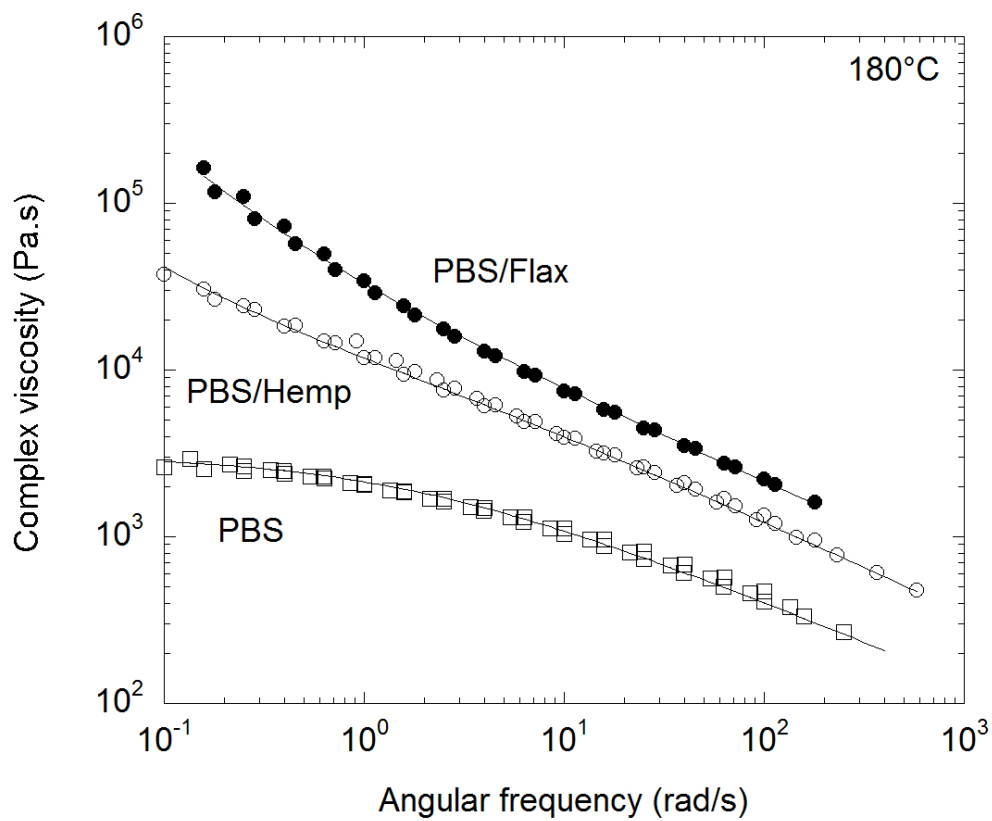


Figure 8. Complex viscosity curves of PBS and PBS-based composites at 180°C. Full lines are fits with a Carreau-Yasuda model.

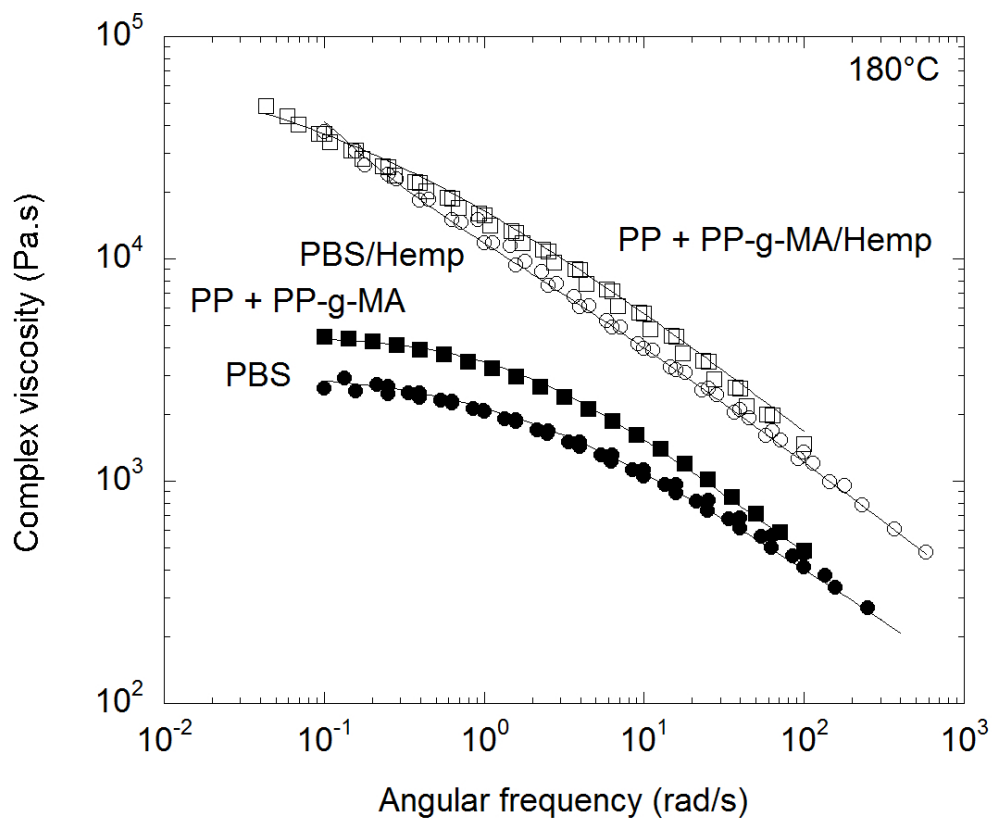


Figure 9. Complex viscosity curves of the two matrices and the corresponding hemp-based composites at 180°C. Full lines are fits with a Carreau-Yasuda model.

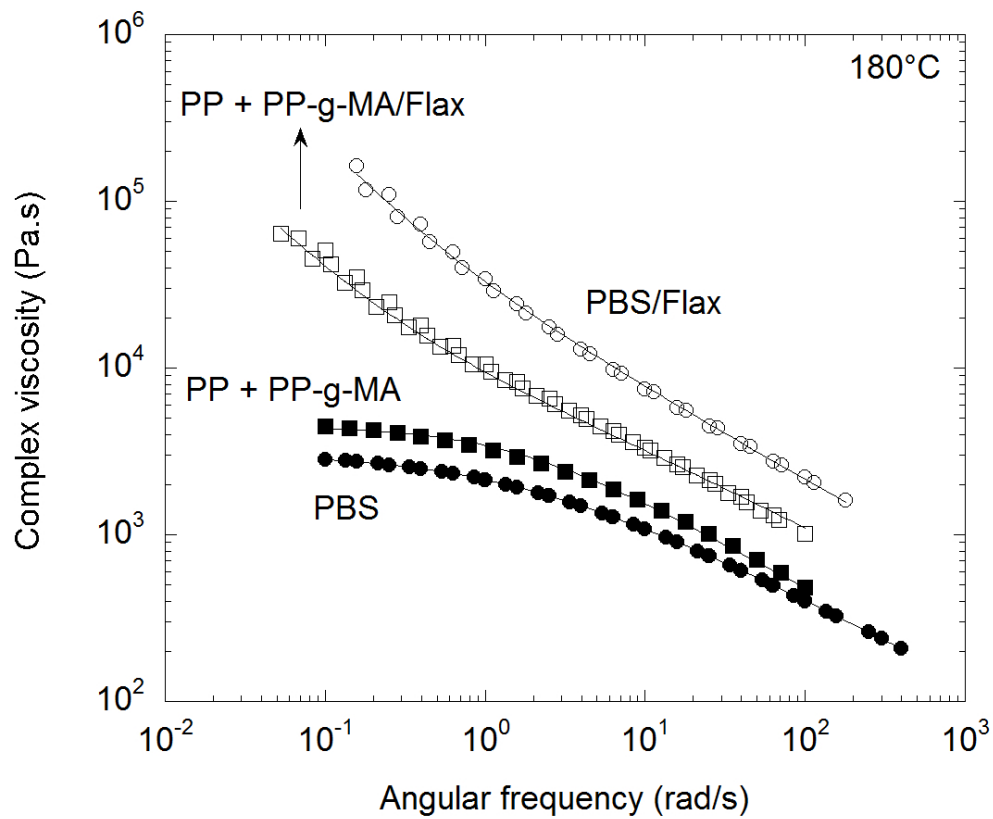


Figure 10. Complex viscosity curves of the two matrices and the corresponding flax-based composites at 180°C. Full lines are fits with a Carreau-Yasuda model.

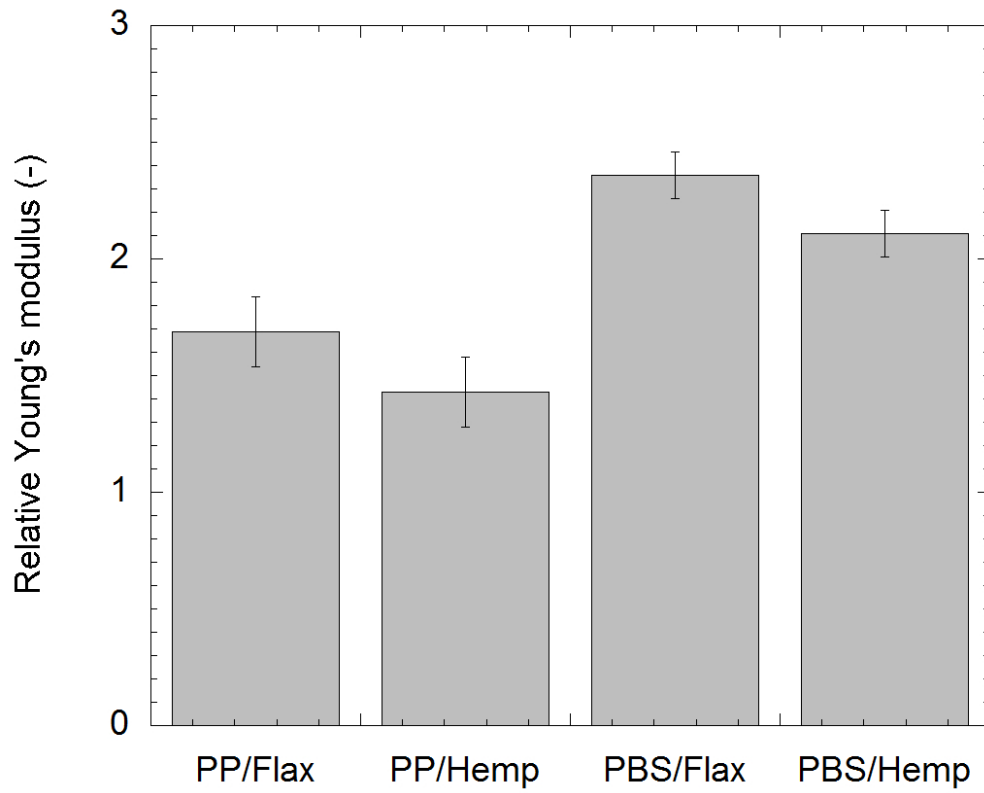


Figure 11. Mechanical properties of the various composites. (a) Relative Young's modulus, (b) Stress at break, (c) Elongation at break. PP means PP/PP-g-MA.

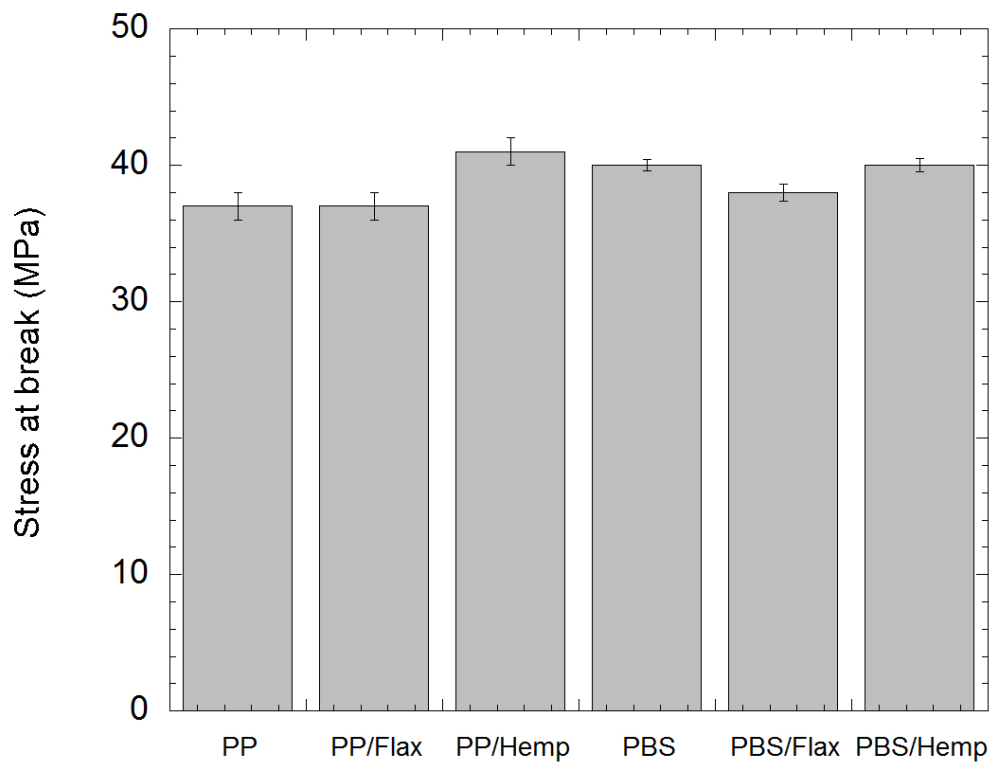


Figure 11. Mechanical properties of the various composites. (a) Relative Young's modulus, (b) Stress at break, (c) Elongation at break. PP means PP/PP-g-MA.

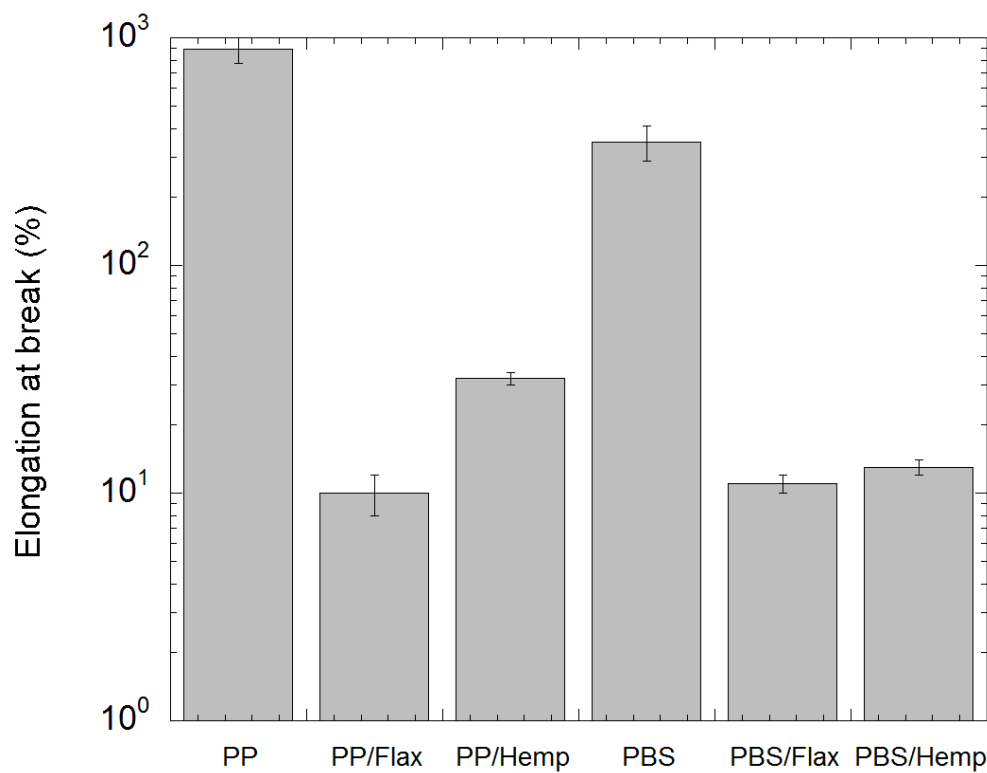


Figure 11. Mechanical properties of the various composites. (a) Relative Young's modulus, (b) Stress at break, (c) Elongation at break. PP means PP/PP-g-MA.

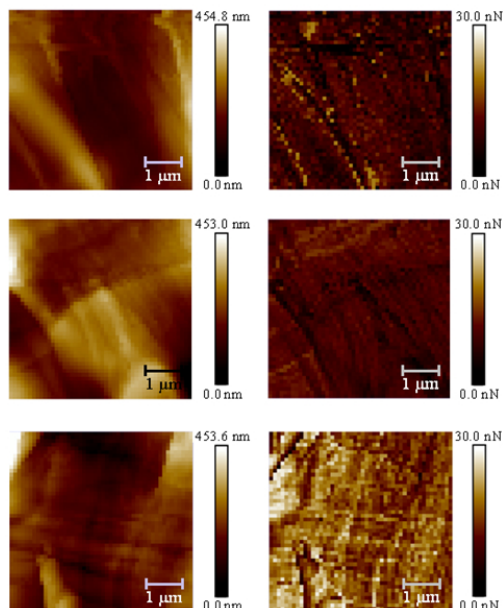


Figure 12. Force spectroscopy experiments between nanocrystalline cellulose-functionalized AFM levers (coverage of nanocrystalline cellulose is  $55.8 \pm 2.6\%$ ). Topography channel (a) and adhesion force map (b) regarding, from top to bottom, PP, PP/PP-g-MA and PBS surfaces. Scan size is  $25 \mu\text{m}^2$  for all sections. Temperature and RH are fixed at  $25^\circ\text{C}$  and  $45\%$ , respectively.

254x190mm (96 x 96 DPI)

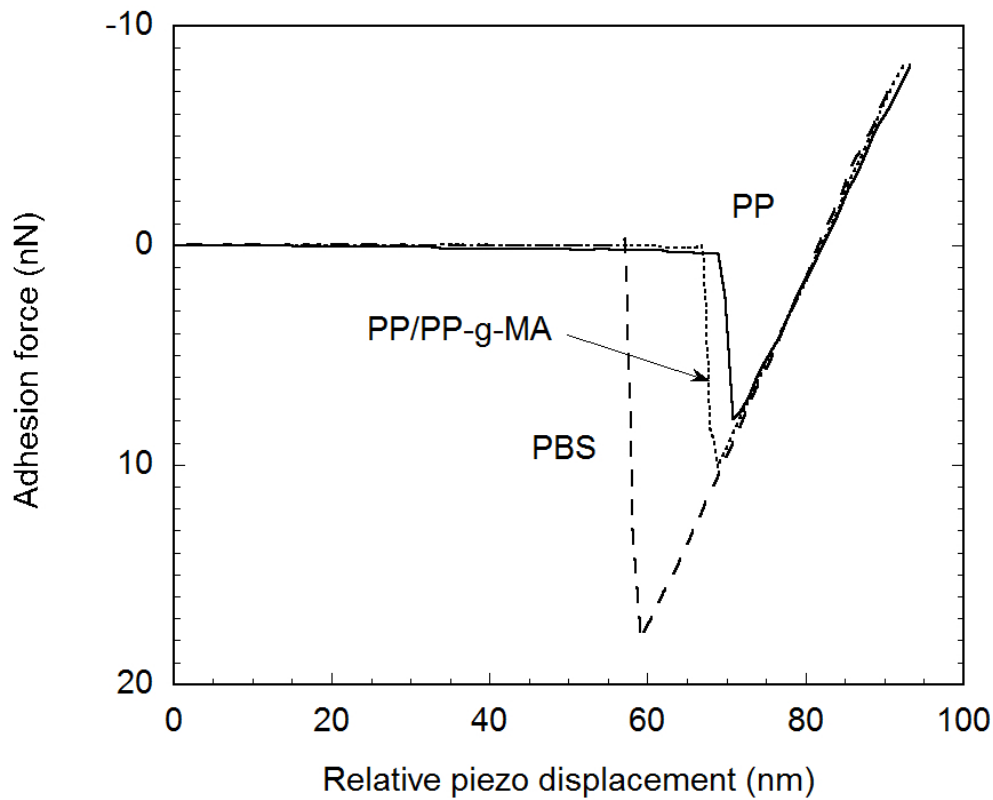


Fig 13

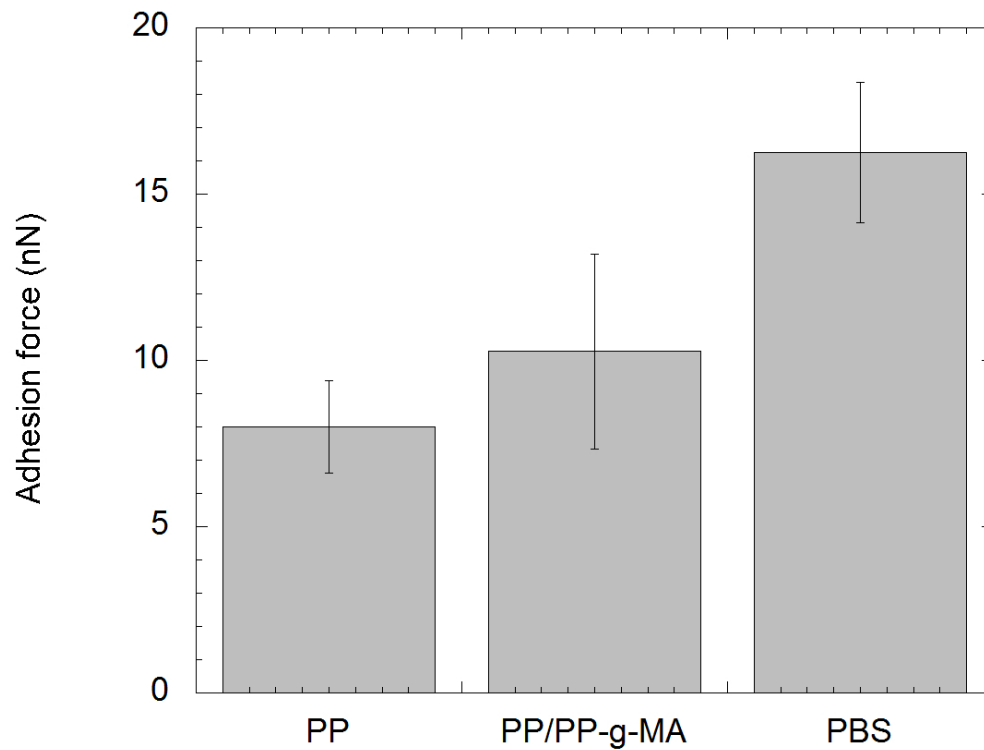


Figure 14. Intermolecular adhesion forces between nanocrystalline cellulose functionalized AFM levers with PP, PP/PP-g-MA and PBS at 25°C and 45% RH.